Joule

CellPress

Article

Solid-state lithium battery cathodes operating at low pressures

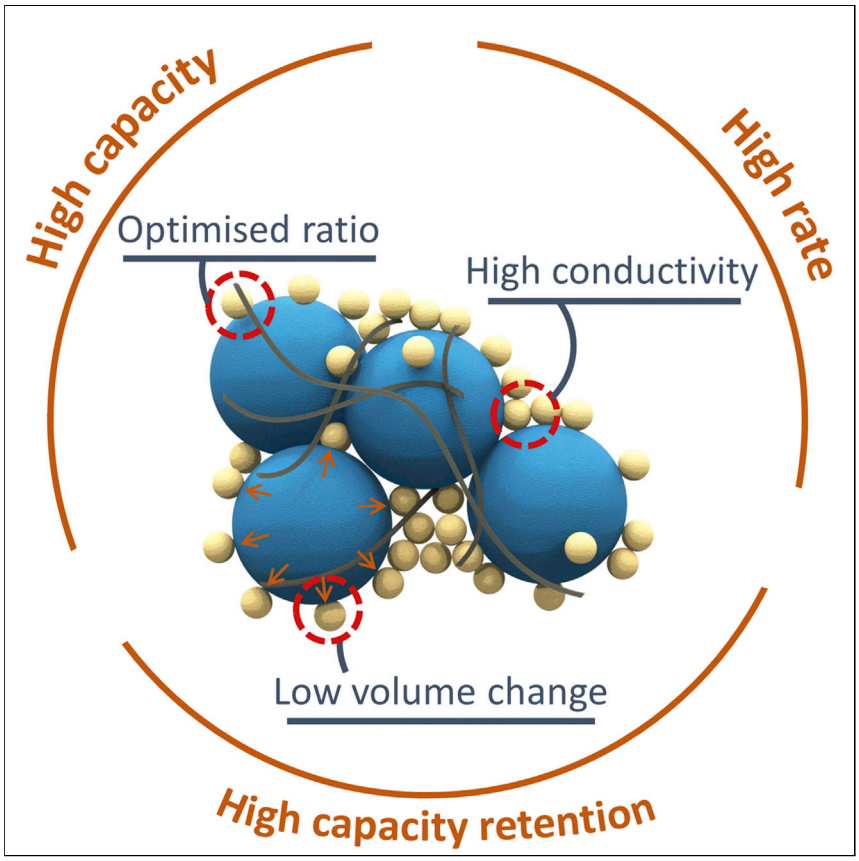

A solid-state composite cathode comprises particles of cathode active materials, solid electrolytes, and often carbon. Here, we show that the capacity depends primarily on the ion transport through the solid electrolyte within the composite cathode. The capacity fades on cycling due to the volume changes of the active materials, which is much more significant at lower pressures. This work suggests solutions to achieve and maintain the high capacity at high rates and low pressures.

Xiangwen Gao, Boyang Liu, Bingkun Hu, ..., David Armstrong, Patrick S. Grant, Peter G. Bruce

peter.bruce@materials.ox.ac.uk

Highlights

The cathode capacity is limited by the conductivity of the solid electrolyte

The capacity fades on cycling due to the volume changes of the active materials

The cathode capacity fades much more significantly at lower pressures

Gao et al., Joule 6, 636–646
March 16, 2022
https://doi.org/10.1016/j.joule.2022.02.008

CellPress

Joule

Article

Solid-state lithium battery cathodes operating at low pressures

Xiangwen Gao,[1] Boyang Liu,[1] Bingkun Hu,[1] Ziyang Ning,[1] Dominic Spencer Jolly,[1] Shengming Zhang,[1] Johann Perera,[1] Junfu Bu,[1] Junliang Liu,[1] Christopher Doerrer,[1] Ed Darnbrough,[1] David Armstrong,[1] Patrick S. Grant,[1] and Peter G. Bruce[1,2,3,*]

SUMMARY

Many studies of solid-state battery cathodes employ high stack pressures and low current densities. In practice, cells operating at current densities in the mA cm^{-2} range at stack pressures of a few MPa are required. Here, we show the influence of the composite cathode components $LiNi_{0.83}Mn_{0.06}Co_{0.11}O_2$, Li_3InCl_6, and carbon nanofibers, operating at 2-MPa stack pressure and find that the overall composite cathode capacity is determined primarily by the conductivity of the solid electrolyte. Higher conductivities reduce the mass of the solid electrolyte required to access a high capacity from the active material (high utilization), enabling higher active material loadings and higher overall capacities. Cycling between 2.6 and 4.2 V rather than 4.4 V reduces the $LiNi_{0.83}Mn_{0.06}Co_{0.11}O_2$ volume change from 6% to 2.5%, achieving 94% rather than 65% capacity retention after 50 cycles for a reduction in capacity of only 14%.

INTRODUCTION

Solid-state lithium batteries, in which the liquid electrolyte is replaced by a lithium-ion-conducting ceramic, offer improved safety and, if the graphite anode is replaced by lithium metal, higher energy density than liquid electrolyte cells.[1–8] However, the substitution of liquid-solid interfaces with solid-solid interfaces presents significant challenges.[9–15] While much attention has been given to the Li anode, the intercalation cathode also presents at least as great a challenge.[16,17] In solid-state cells, the cathode is a composite comprising particles of the cathode active material (CAM), the solid electrolyte (SE), and often carbon. To maximize energy density, a high loading of the CAM per unit electrode area is desirable. However, even in liquid electrolyte cells, the cathode must sacrifice some degree of loading to provide porosity into which the liquid electrolyte floods ensuring sufficient mass transport of Li^+ to and from the CAM to deliver adequate charge/discharge rates. Similarly, carbon is often added to the electrode to ensure good electronic transport between the current collector and the CAM particles. The all-solid-state nature of the composite makes the realization of the cathode more difficult than that in liquid cells.[18,19] In the latter, the liquid electrolyte readily wets CAM particle surfaces and remains in intimate contact even when the active particles expand and contract on cycling. In contrast, in solid-state cells, maintaining interparticle contact, whether between the particles of the SE and the CAM or between the SE particles themselves, is more difficult. A number of studies have been carried out to explore solid-state cathodes. Recent work by Minnmann et al.[20] considered the effect of the ion and electron transport numbers on the composite cathode behavior. Work by Shi et al.[21] explored

Context & scale

Solid-state lithium-metal batteries have the potential to offer improved safety and higher energy density than current lithium-ion batteries. Many studies use high stack pressures and low current densities to avoid many problems of complex solid-state cathodes at the expense of the relevance to practical applications. Here, we consider the factors that affect the solid-state cathode performance under relatively low pressures and high rates. We show the capacity that can be obtained from the cathode depends primarily on the ion transport through the solid electrolyte within the composite. The capacity fades on cycling due to the volume changes of the active materials. This work highlights the importance of finding highly conducting solid electrolytes to deliver high capacities at high rates and low stack pressures. It reinforces the need for active materials with zero or very low volume change or strategies that could mitigate the problems of volume change during cycling.

the relative particle sizes between SEs and the CAMs. Han et al.[22] compared the cell performance based on single- or polycrystalline CAMs with sulfide- or halide-based SEs. Together, these papers show the complexity of solid-state cathodes. Many studies of solid-state batteries (SSBs) use high stack pressures, in some cases in excess of 250 MPa, and commonly use relatively low current densities. By doing so, many problems of solid-state cathodes can be avoided but at the expense of relevance to practical cells.[23–26] Such high pressures may prove difficult or expensive to achieve.

Here, we consider the factors that affect achieving high-capacity solid-state cathodes and sustaining the high capacity while operating under relatively low pressures of between 1 and 2 MPa and at a current density of 1 mA cm^{-2}. It should be noted that lower pressures may be required in some applications. Thiophosphate-based electrolytes are a strong focus for all-SSBs due to their combination of good conductivity and more compliant mechanical properties than oxides.[20,27–29] However, such electrolytes are unstable toward the oxidizing potentials of typical CAMs, necessitating coating of the CAM particles, which further complicates understanding the fundamental factors that influence the performance of solid-state cathodes, especially since here we wish to investigate the capacity retention on cycling. As a result, we used chloride-based SEs, principally Li_3InCl_6, as our SE. It has been shown to be able to operate at the potentials of typical CAMs, such as the intercalation cathode material $LiNi_{0.83}Mn_{0.06}Co_{0.11}O_2$ (NMC) used in this work, and the addition of carbon does not result in SE decomposition.[30–33] We show the capacity that can be obtained from the composite cathode depends primarily on the ion transport through the SE within the composite, i.e., the SE conductivity. More highly conducting SEs permit a higher degree of CAM loading (less SE is required in the cathode to maintain ion transport) while still maintaining high utilization of the active materials, resulting in a high overall composite cathode capacity. Using Li_3InCl_6 as the SE, 210 mA h g^{-1} can be stored in the single-crystal $LiNi_{0.83}Mn_{0.06}Co_{0.11}O_2$ CAM on the first cycle between 2.6 and 4.4 V at 2-MPa stack pressure, 1 mA cm^{-2}, and 80°C, which is the same capacity (utilization) for $LiNi_{0.83}Mn_{0.06}Co_{0.11}O_2$ in a liquid electrolyte cell at room temperature. The capacity fades on cycling due to the volume changes of the CAM. High pressures used in many studies of SSBs mask or overcome this effect by pressing the particles back into contact; the capacity fade of SSBs is much more significant at low pressures.[34] However, by using 4.2 V instead of a 4.4 V cutoff, the volume change of the CAM is reduced from approximately 6% to 2.5%, and a capacity retention of 94% rather than 65% was obtained after 50 cycles for a reduction in capacity of only 14%. This work highlights the imperative of finding highly conducting SEs to reduce the amount of SE in the composite cathode, thereby increasing the CAM loading to deliver high capacities at high rates, low stack pressures, and ambient temperatures. It also reinforces the need for CAMs with zero or very low volume change on cycling or the exploration of other strategies that could mitigate the problems of volume change of CAMs during cycling.

RESULTS AND DISCUSSION

Li_3InCl_6 was synthesized by ball milling as based on previous studies, as described in experimental procedures.[33] Powder X-ray diffraction (PXRD) showed Li_3InCl_6 to be a single-phase product, Figure S1. Compared with oxides, it has a relatively low elastic modulus (34.2 $\pm$ 0.8 GPa) and hardness (2.07 $\pm$ 0.10 GPa) and therefore a similar compliance to sulfides, as shown in Table S1. Solid-state cells were assembled as described in experimental procedures and shown in Figure S2. The composite cathode consisted of Li_3InCl_6 as the SE, single-crystal $LiNi_{0.83}Mn_{0.06}Co_{0.11}O_2$ as the CAM, and carbon nanofibers (CNFs). Scanning electron microscopy (SEM) images

[1]Department of Materials, University of Oxford, Oxford OX1 3PH, UK

[2]Department of Chemistry, University of Oxford, Oxford, UK

[3]Lead contact

*Correspondence: peter.bruce@materials.ox.ac.uk

https://doi.org/10.1016/j.joule.2022.02.008

show average particle sizes of several hundred nanometers for Li_3InCl_6, 1–5 μm for the CAM, and 50- to 200-nm diameters for the CNF (Figure S3). Single-crystal $LiNi_{0.83}Mn_{0.06}Co_{0.11}O_2$ used in this study has been shown recently to sustain pressures of 500 MPa without cracking. The absence of CAM cracking is confirmed by the cross-sectional SEM image of the composite cathode in Figure S4.[34] A layer of Li_3InCl_6 is located adjacent to the cathode, and a further layer of Li_6PS_5Cl is placed between this and the Li-In alloy acting as the second electrode. Li_3InCl_6 is unstable when in contact with the reducing anode, and the inclusion of Li_6PS_5Cl avoids this problem.[30,35] The impedance between the two SEs is low.[35] The use of Li-In alloy enables access to the current density of 1 mA cm^{-2} on cycling without dendrite formation (0.6 V versus Li^+/Li). The composite electrodes were approximately 70 μm thick without including the current collector, except where otherwise stated.

To reach an areal capacity of 3 mA h cm^{-2}, a 70-μm-thick cathode was constructed with ~14 mg cm^{-2} CAM mass loading and mass ratios of CAM:SE:CNF of 65:30:5, corresponding to volume ratios of 49:41:10, respectively.[23,36] The voltage profile of the first cycle, as shown in Figures 1 and S5, shows the effect of doubling the current density from 0.5 to 1 mA cm^{-2}, changing the pressure from 2 to 10 Mpa and increasing temperature from 30°C to 80°C. The capacity of this CAM in liquid electrolyte cells at 30°C is typically around 210 mA h g^{-1}_{CAM}. It is evident that a current density of 1 mA cm^{-2} cannot be obtained at 30°C under 2 MPa. At 30°C, it is only possible to approach this utilization (capacity) of the CAM at 0.5 mA cm^{-2} under 10 MPa. However, increasing the temperature to 80°C does permit utilization of 210 mA h g^{-1}_{CAM} at 1 mA cm^{-2} under 2 MPa, comparable to that in liquid electrolyte cells at room temperature, suggesting that the inferior capacity at 30°C for the solid-state cathode is not limited by the mass transport within the CAM but the SE conductivity. If we take account of the mass of the whole composite cathode, it corresponds to a capacity of ~137 mA h g^{-1}_{total} and an areal capacity of 3 mA h cm^{-2}. To systematically investigate how the presence of carbon, the ratio of SE to CAM, and the conductivity of the SE influence the capacity that can be obtained from the composite cathode, the following studies were carried out at 80°C under 2 MPa.

The effect of adding carbon to the solid-state cathode is shown in Figure 2. We start from the composite cathode ratio used in Figure 1 and then vary the carbon content. Li_3InCl_6 is known to be stable when operating at the potentials of typical CAMs.[33] In these experiments, the ratio of CAM to SE was constant as the CNF percentage was varied from 1 wt % CNF to 10 wt % CNF. The variation expressed as a function of the cathode volume is shown in Figure S6. The highest capacity is obtained with 5 wt % CNF, corresponding to a utilization of 210 mA h g^{-1}_{CAM}. We express the capacity obtained based on the total mass of the cathode since here and in the results presented in subsequent sections, the mass of CAM varies, and it is the capacity per total cathode mass that matters ultimately. The increase in thickness of the cathode from 5 to 10 wt % CNF cannot explain the lower capacity, as the electrode thickness only increased from 70 to 80 μm. Significantly lower CNF percentages do not provide sufficient electronically conducting pathways through the composite electrode to ensure activity of a high proportion of the CAM, while higher proportions of carbon may disrupt ionic pathways in the composite cathode. The quantity of carbon required will of course depend on the electronic conductivity of the CAM used in the composite cathode. The addition of carbon is important in the case of the NMC family, as their electronic conductivities are typically below 3×10^{-5} S cm^{-1}. This is not the case for studies of SSBs employing $LiCoO_2$, as $LiCoO_2$ has a much higher electronic conductivity of 1×10^{-3} S cm^{-1}.[33,37–40]

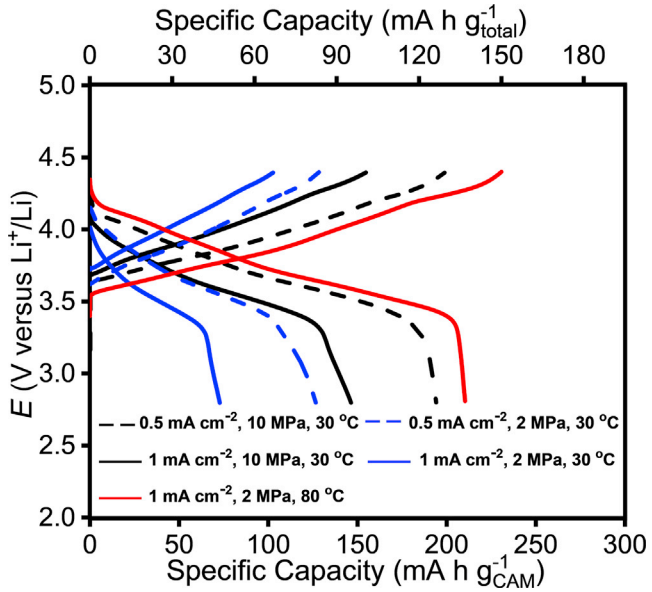

Figure 1. Comparisons of the first cycle performance of the composite cathode under different current densities and stack pressures

Load curves for the first cycle of the composite cathode with current densities of 0.5 mA cm^{-2} (dashed line) and 1 mA cm^{-2} (solid line) under stack pressures of 2 MPa (blue) to 10 MPa (black) at 30°C, compared with 1 mA cm^{-2} under 2 MPa at 80°C (red). The CAM, SE, and CNF mass ratios are 65 wt %, 30 wt %, and 5 wt %, respectively. The bottom x axis is the specific capacity calculated based on the mass of the CAM, and the top x axis is the specific capacity calculated based on the mass of the total composite cathode.

The effect of changing the SE content in the composite cathode is shown in Figure 3, where the same proportion of carbon is present in all cases. Therefore, an increased loading of CAM corresponds to a lower quantity of the SE in the composite cathode. We start from the 65 wt % of CAM used in Figure 1, since it gives a utilization of 210 mA h g^{-1}_{CAM}, comparable to that in liquid cells. Increasing the loading of CAM beyond 65 wt % reduces the capacity. Even a modest increase in the CAM loading from 65 to 70 wt % reduces the capacity to some extent. The results show that despite the higher amount of CAM, the reduced amount of SE results in a lower utilization (capacity) of the CAM at a current density of 1 mA cm^{-2} under a stack pressure of 2 MPa at 80°C. The trend with the volume of cathode is the same and shown in Figure S7. The results suggest that the conductivity of the SE is limiting the capacity and hence energy density of the solid-state cathode.

To confirm the important role of SE conductivity in accessing the capacity of the CAM in the composite solid-state cathode, cells were constructed with three different chloride-based SEs with similar oxidation stability as shown previously: $LiAlCl_4$, Li_3YCl_6, and Li_3InCl_6.[41–43] These SEs were synthesized by ball milling, as detailed in experimental procedures. The PXRD in Figures S1 and S8 showed that all three chloride-based SEs are single-phase products, and SEM images in Figures S3 and S9 demonstrated that these SEs have similar particle sizes. Symmetric cells with blocking electrodes, such as carbon that ensures good contact, are used widely to determine the ionic conductivities of materials that are predominately ionic conductors, including halide-based SEs.[44,45] The impedance of the C|Li_3InCl_6|C cell was measured at −20°C to observe high-frequency contributions, as shown in Figure S10; however, the bulk (intracrystalline) and grain boundary (intercrystalline) contributions could not be resolved. Therefore, at this and higher temperatures, we

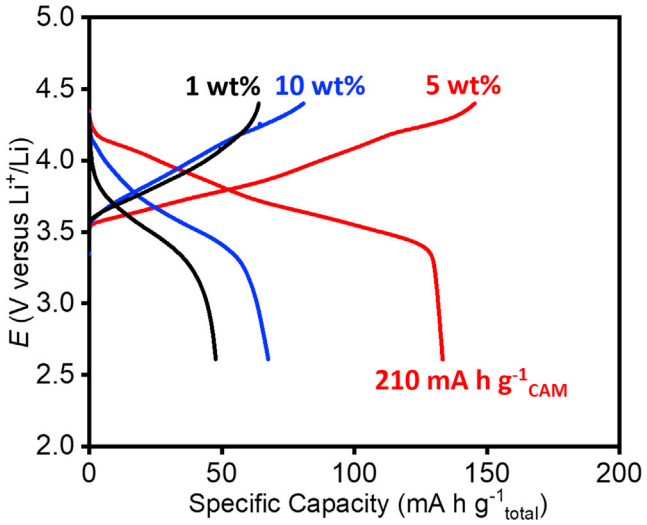

Figure 2. Load curves for the first cycle of the composite cathode with different CNF mass ratios
1 wt % (black), 5 wt % (red), and 10 wt % (blue) under 2 MPa at 80°C. The mass ratio of CAM to SE is constant at 13:6. The current density is 1 mA cm^{-2}. The specific capacity is calculated based on the mass of the total composite cathode. The cathode with 5 wt % CNF represents a CAM utilization of 210 mA h g^{-1}_{CAM}.

extract the total resistance from the high-frequency x axis intercept of the linear impedance to calculate the conductivity of the SE pellet, and their conductivities are 0.16 mS cm^{-1} ($LiAlCl_4$), 1.3 mS cm^{-1} (Li_3YCl_6), and 2 mS cm^{-1} (Li_3InCl_6) under 2 MPa at 80°C. The composite cathodes were then made with the same volume ratio of CAM, chloride-based SEs, and CNFs, which, along with similar particle sizes, ensure similar particle contacts. Cells with each electrolyte were cycled under a stack pressure of 2 MPa at 80°C. To demonstrate the performance of the composite cathode in practical cells with thinner electrolyte separator layers than used here, i*R compensation was applied to correct for the effect of the voltage drop associated with a 100-μm-thick SE layer. The results (specific and volumetric capacity comparisons) are shown in Figures 4 and S11 for two different composite cathode thicknesses of 70 and 115 μm, respectively. In the case of the 70 μm electrode, the same gravimetric capacity and almost the same volumetric capacity (Figure S11) is obtained for the two electrolytes with conductivities of 1.3 and 2 mS cm^{-1}, but the SE with the lowest conductivity, 0.16 mS cm^{-1}, shows a significantly lower capacity. The thicker the electrode, the more charge transport limits the accessible capacity. For Li_3InCl_6 with a conductivity of 2 mS cm^{-1}, the 115-μm-thick electrode achieves an areal capacity of 5 mA h cm^{-2}, with a utilization of the CAM of 210 mA h g^{-1}_{CAM}, while a decrease in the conductivity from 2 to 1.3 mS cm^{-1} reduces the capacity that can be accessed, and the cathode with the SE of 0.16 mS cm^{-1} has a very low capacity. These results and those above highlight the significance of SE conductivity in terms of being able to tolerate a high loading of CAM and high utilization, leading to a high overall electrode capacity.

The conductivity of Li_3InCl_6 is pressure dependent, which increases from 0.35 mS cm^{-1} (2 MPa) to 0.52 mS cm^{-1} (10 MPa) at 30°C, as shown in Figure S12. This is not related to the contact between the electrodes used to measure the conductivity and the SE, since the same pressure dependence is observed with carbon and in metal electrodes. This pressure dependence is not observed in Li_6PS_5Cl, as shown in Figure S12, which is in accordance with previous studies, further confirming that

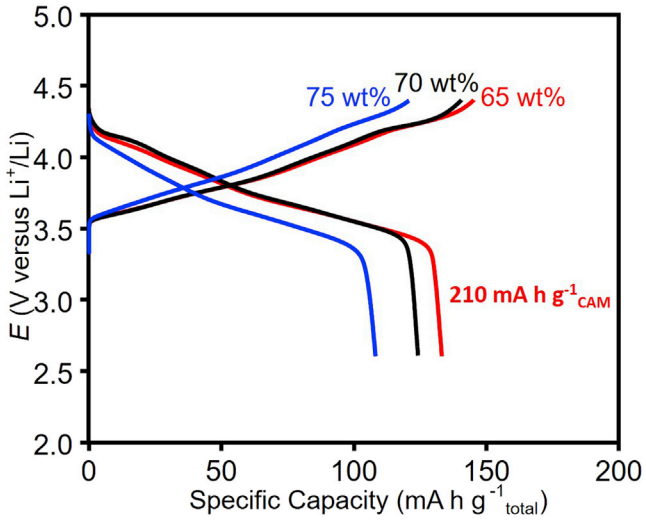

Figure 3. Load curves for the first cycle of the composite cathode with different CAM ratios
65 wt % (red), 70 wt % (black), and 75 wt % (blue) under 2 MPa at 80°C. The carbon mass ratio is fixed at 5 wt %. The current density is 1 mA cm^{-2}. The specific capacity is calculated based on the mass of the total composite cathode. The cathode with 65 wt % CAM represents a utilization of 210 mA h g^{-1}_{CAM}.

the pressure-dependent conductivity is a property of Li_3InCl_6.[44] The pressure has been linked to the improved interparticle contact in the SE at higher pressures, and we anticipate that the effect of pressure is on the grain boundary resistance.[44,46] However, the bulk and the grain boundary resistance cannot be deconvoluted in the impedance spectrum, as shown in Figure S10, preventing precise assignment of the pressure dependence. The higher conductivity will translate into better composite cathode performance if higher stack pressures are applied to the cell. However, the effect of pressure is more significant on the capacity retention during cycling, as discussed next. The capacity retention of cells cycled at 1 mA cm^{-2} under 2 MPa at 80°C and between 2.6 and 4.4 V is shown in Figure 5A. After 50 cycles, the discharge capacity was only 65% of that after the first cycle. The microstructure change in the composite cathode was examined using plasma focused ion beam SEM (PFIB-SEM), as detailed in experimental procedures. The composite cathode was milled out, and a series of parallel cross-sectional SEM images were taken equidistantly with a separation of 100 nm between the image slices. The resultant image stack was cropped, aligned, and processed for segmentation of the composite cathode components and 3D visualization. The reconstructed structures of the composite cathodes before and after 50 cycles are shown in Figures 5B and 5C, where CAM (green), Li_3InCl_6 (purple), CNF (orange), and void (black) can be seen as clearly separated. Before cycling, the voids in the composite cathode are very small, as shown in Figure 5B, while in contrast, after 50 cycles, the volume fraction and size of voids increased significantly, corresponding to reduced interparticle contact in accordance with the capacity fade observed during cycling.

Increasing the stack pressure to 10 MPa resulted in a modest increase of the first discharge capacity, i.e., 141 $\pm$ 0.6 mA h g^{-1}_{total}. More importantly, markedly superior capacity retention (93% $\pm$ 0.6% after 50 cycles) was observed, as shown in Figures 6A and S13, suggesting that the increased pressure retains the morphology of the pristine cathode with its intimate particle contact. SEM reconstructions of the cathode charged to 4.4 V at 10 MPa are shown in Figure 6B and are consistent

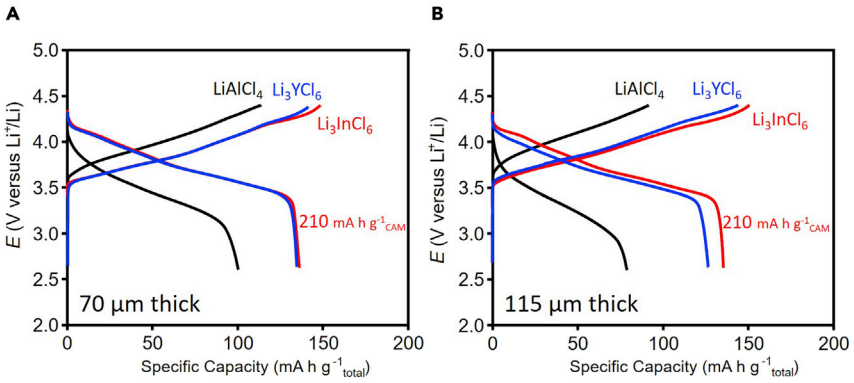

Figure 4. Load curves of the first cycle of the composite cathode with various SEs: Li_3InCl_6 (red), Li_3YCl_6 (blue), and $LiAlCl_4$ (black) under 2 MPa at 80°C

The current density is 1 mA cm^{-2}. The cathode with Li_3InCl_6 represents a utilization of 210 mA h g^{-1}_{CAM}. The specific capacity is calculated based on the mass of the total composite cathode. iR compensations are applied. The CAM, SE, and CNF volume ratios are 49%, 41%, and 10%, respectively.

(A and B) The loading thickness is (A) 70 µm and (B) 115 µm.

with retention of the intimate particle contact, reinforcing the importance of retaining the composite cathode microstructure on cycling. To explore this further, cells were cycled at 1 mA cm^{-2} and 80°C under 2 MPa stack pressure but at a lower cutoff voltage of 4.2 V, as shown in Figures 6C and S14. Although the capacity decreased by 14% from 137 mA h g^{-1}_{total} to 118 mA h g^{-1}_{total}, a marked improvement in capacity retention was observed, i.e., 94% $\pm$ 1.2% after 50 cycles at a low pressure of 2 MPa with good particle contact shown in SEM reconstructions (Figure 6D). Of the three components that make up the composite cathode, the CAM contracts on charging (lithium de-intercalation) and expands on discharge (lithium intercalation). The volume change of single-crystal NMC when charged to 4.4 V is around 6%, whereas it is only 2.5% when charged to 4.2 V as shown in Figure 6B.[28,47] The superior capacity retention on cycling with reduced volume change of the CAM even at 2 MPa pressure is also consistent with the importance of maintaining microstructure on cycling. This is further reinforced when, after charging to 4.4 V galvanostatically under 2 MPa, 15 min of a voltage hold was imposed (Figure S15). This shows improved capacity retention (89%) compared with the same cycling conditions without the voltage hold, consistent with the composite cathode morphology relaxing when held at the top of charge to re-establish particle contacts. The variation of performance with pressure, and the observation that limiting the cutoff voltage and therefore volume change to 2.5% or less greatly improves capacity retention, demonstrates the importance of discovering CAMs or introducing a flexible buffer layer to ensure good contact during cycling if a composite cathode is to operate at a practical pressure.

Conclusions

The composite cathode of an SSB presents several challenges. The capacity of the composite cathode is limited by the conductivity of the SE. Higher SE conductivity reduces the amount of solid electrolytes required to access the active material capacity (utilization), enabling higher active material loading and therefore higher overall capacity of the composite cathode. In the case of $LiNi_{0.83}Mn_{0.06}Co_{0.11}O_2$ studied here, a 70-µm-thick composite cathode utilizing Li_3InCl_6 as the SE in a cell operated at 1 mA cm^{-2} and 80°C under 2-MPa stack pressure is limited to a CAM

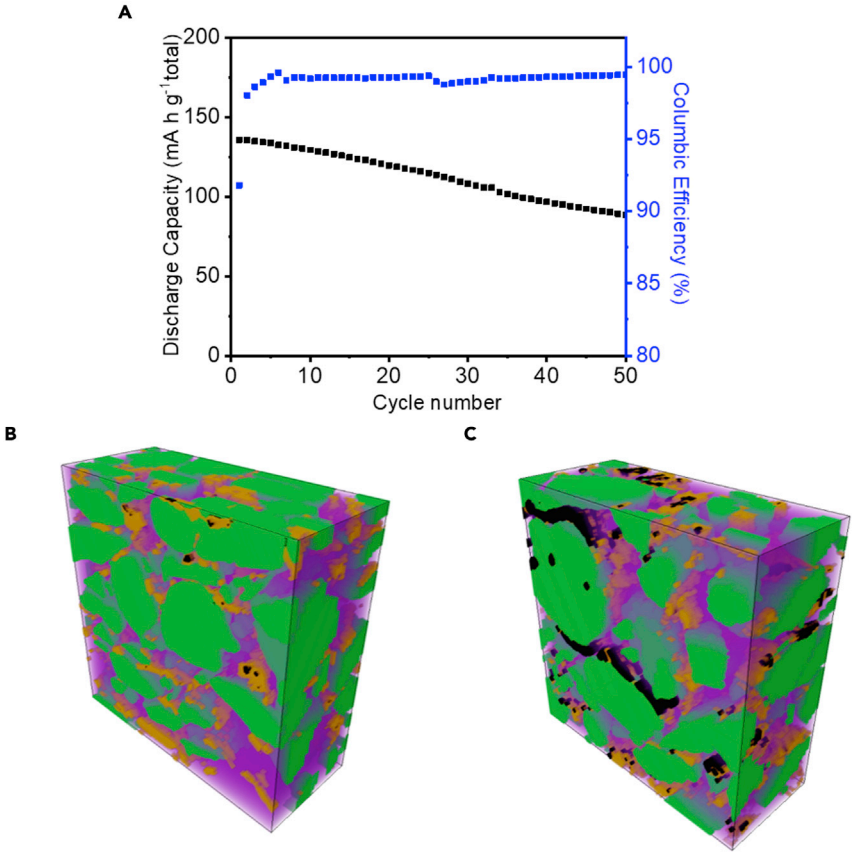

Figure 5. The cycling performance and the corresponding reconstructed 3D morphology of the composite cathode when charged to 4.4 V under 2 MPa

(A) Cycling performance of the composite cathode between 2.6 and 4.4 V under 2 MPa at 80°C. The current density is 1 mA cm^{-2}. The CAM, SE, and CNF mass ratios are 65 wt %, 30 wt %, and 5 wt %, respectively.

(B and C) Reconstructed 3D structures of the (B) pristine cathode composite and (C) after 50 cycles (green: NMC, purple: Li_3InCl_6, orange: CNF, black: void). The reconstructed volume is 5.8 μm × 5.8 μm × 2.5 μm.

loading of 65 wt % in order to achieve a high utilization of the active material (210 mA h g^{-1}). Increasing the thickness from 70 to 115 μm with the same conditions permits the same utilization and can reach an areal capacity of 5 mA h cm^{-2}. Limiting the volume change of the CAM to approximately 2.5% (2.6–4.2 V) rather than 6% (2.6–4.4 V) raises the capacity retention on cycling from 65% to 94% at 2-MPa stack pressure. In terms of future research, solid electrolytes with higher conductivity are an important goal if the maximum capacity is to be obtained at realistic current densities at room temperatures or lower and under even lower stack pressures than 2 MPa for some applications. Intercalation compounds with a low volume change and a flexible buffer layer to ensure good contact in the composite cathode can significantly improve capacity retention at lower pressures.

EXPERIMENTAL PROCEDURES

Resource availability

Lead contact

Further information and requests for resources should be directed to and will be fulfilled by the lead contact, Peter G. Bruce (peter.bruce@materials.ox.ac.uk).

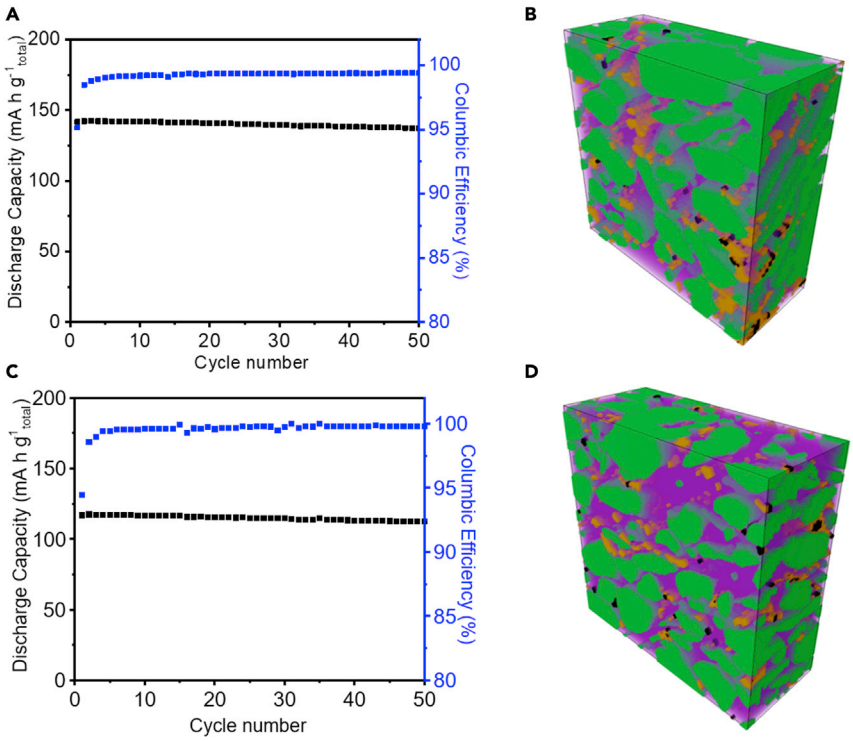

Figure 6. The cycling performance and the corresponding reconstructed 3D morphology of the composite cathode with a higher pressure or a lower cutoff voltage

(A and B) (A) Cycling performance of the composite cathode with a cutoff voltage of 4.4 V and stack pressure of 10 MPa and (B) its corresponding reconstructed 3D structure after 50 cycles.

(C and D) (C) Cycling performance of the composite cathode with a cutoff voltage of 4.2 V and stack pressure of 2 MPa and (D) its corresponding reconstructed 3D structure after 50 cycles. The CAM, SE, and CNF mass ratios are 65, 30, and 5 wt %, respectively. All cells were cycled at 80°C with a current density of 1 mA cm^{-2}. The reconstructed volume is 5.8 μm × 5.8 μm × 2.5 μm (green: NMC, purple: Li_3InCl_6, orange: CNF, black: void).

Materials and availability

This study did not generate new unique materials.

Data and code availability

The data that support the findings of this study are available from the corresponding author upon reasonable request. Full details of experimental procedures can be found in supplemental information.

SUPPLEMENTAL INFORMATION

Supplemental information can be found online at https://doi.org/10.1016/j.joule.2022.02.008.

ACKNOWLEDGMENTS

P.G.B. is indebted to the Faraday Institution SOLBAT (FIRG007 and FIRG008), as well as the Engineering and Physical Sciences Research Council, Enabling Next Generation Lithium Batteries (EP/M009521/1), the University of Oxford experimental equipment upgrade (EP/M02833X/1), and the Henry Royce Institute for Advanced Materials (EP/R0066X/1, EP/S019367/1, and EP/R010145/1) for financial support.

AUTHOR CONTRIBUTIONS

X.G. designed the experiments. C.D. and X.G. designed the cells. X.G. and B.L. performed electrochemical measurements; X.G., B.L., S.Z., and J.B. performed microscopy imaging; and B.H., Z.N., and J.L. conducted the imaging reconstruction. J.P., E.D., and D.A. performed the mechanical property analysis. X.G., B.L., B.H., D.S.J., S.Z., C.D., D.A., and P.S.G. interpreted the data. X.G. and P.G.B. wrote the paper with contributions from all authors.

DECLARATION OF INTERESTS

The authors declare no competing interests.

Received: September 19, 2021
Revised: October 20, 2021
Accepted: February 16, 2022
Published: March 16, 2022

REFERENCES

1. Janek, J., and Zeier, W.G. (2016). A solid future for battery development. Nat. Energy *1*, 16141.
2. Famprikis, T., Canepa, P., Dawson, J.A., Islam, M.S., and Masquelier, C. (2019). Fundamentals of inorganic solid-state electrolytes for batteries. Nat. Mater. *18*, 1278–1291.
3. Tian, Y., Zeng, G., Rutt, A., Shi, T., Kim, H., Wang, J., Koettgen, J., Sun, Y., Ouyang, B., Chen, T., et al. (2021). Promises and challenges of next-generation "Beyond Li-ion" batteries for electric vehicles and grid decarbonization. Chem. Rev. *121*, 1623–1669.
4. Wang, M.J., Kazyak, E., Dasgupta, N.P., and Sakamoto, J. (2021). Transitioning solid-state batteries from lab to market: linking electro-chemo-mechanics with practical considerations. Joule *5*, 1371–1390.
5. Cheng, X.B., Zhao, C.Z., Yao, Y.X., Liu, H., and Zhang, Q. (2019). Recent advances in energy chemistry between solid-state electrolyte and safe lithium-metal anodes. Chem *5*, 74–96.
6. Gao, X., Zhou, Y.N., Han, D., Zhou, J., Zhou, D., Tang, W., and Goodenough, J.B. (2020). Thermodynamic understanding of Li-dendrite formation. Joule *4*, 1864–1879.
7. Liu, M., Wang, C., Cheng, Z., Ganapathy, S., Haverkate, L.A., Unnikrishnan, S., and Wagemaker, M. (2020). Controlling the lithium-metal growth to enable low-lithium-metal-excess all-solid-state lithium-metal batteries. ACS Materials Lett *2*, 665–670.
8. Krauskopf, T., Richter, F.H., Zeier, W.G., and Janek, J. (2020). Physicochemical concepts of the lithium metal anode in solid-state batteries. Chem. Rev. *120*, 7745–7794.
9. Kerman, K., Luntz, A., Viswanathan, V., Chiang, Y.-M., and Chen, Z. (2017). Review—practical challenges hindering the development of solid state Li ion batteries. J. Electrochem. Soc. *164*, A1731–A1744.
10. Chen, R., Li, Q., Yu, X., Chen, L., and Li, H. (2020). Approaching practically accessible solid-state batteries: stability issues related to solid electrolytes and interfaces. Chem. Rev. *120*, 6820–6877.
11. Banerjee, A., Wang, X., Fang, C., Wu, E.A., and Meng, Y.S. (2020). Interfaces and interphases in all-solid-state batteries with inorganic solid electrolytes. Chem. Rev. *120*, 6878–6933.
12. Xia, S., Wu, X., Zhang, Z., Cui, Y., and Liu, W. (2019). Practical challenges and future perspectives of all-solid-state lithium-metal batteries. Chem *5*, 753–785.
13. Wang, D., Zhu, C., Fu, Y., Sun, X., and Yang, Y. (2020). Interfaces in garnet-based all-solid-state lithium batteries. Adv. Energy Mater. *10*, 2001318.
14. Albertus, P., Anandan, V., Ban, C., Balsara, N., Belharouak, I., Buettner-Garrett, J., Chen, Z., Daniel, C., Doeff, M., Dudney, N.J., et al. (2021). Challenges for and pathways toward Li-metal-based all-solid-state batteries. ACS Energy Lett. *6*, 1399–1404.
15. Xu, B., Li, X., Yang, C., Li, Y., Grundish, N.S., Chien, P.H., Dong, K., Manke, I., Fang, R., Wu, N., et al. (2021). Interfacial chemistry enables stable cycling of all-solid-state Li metal batteries at high current densities. J. Am. Chem. Soc. *143*, 6542–6550.
16. Pasta, M., Armstrong, D., Brown, Z.L., Bu, J., Castell, M.R., Chen, P., Cocks, A., Corr, S.A., Cussen, E.J., Darnbrough, E., et al. (2020). 2020 roadmap on solid-state batteries. J. Phys. Energy *2*, 032008.
17. Xu, L., Tang, S., Cheng, Y., Wang, K., Liang, J., Liu, C., Cao, Y.C., Wei, F., and Mai, L. (2018). Interfaces in solid-state lithium batteries. Joule *2*, 1991–2015.
18. Nie, K., Hong, Y., Qiu, J., Li, Q., Yu, X., Li, H., and Chen, L. (2018). Interfaces Between cathode and electrolyte in solid state lithium batteries: challenges and perspectives. Front. Chem. *6*, 616.
19. Wang, L., Xie, R., Chen, B., Yu, X., Ma, J., Li, C., Hu, Z., Sun, X., Xu, C., Dong, S., et al. (2020). In-situ visualization of the space-charge-layer effect on interfacial lithium-ion transport in all-solid-state batteries. Nat. Commun. *11*, 5889.
20. Minnmann, P., Quillman, L., Burkhardt, S., Richter, F.H., and Janek, J. (2021). Editors' choice—quantifying the impact of charge transport bottlenecks in composite cathodes of all-solid-state batteries. J. Electrochem. Soc. *168*, 040537.
21. Shi, T., Tu, Q., Tian, Y., Xiao, Y., Miara, L.J., Kononova, O., and Ceder, G. (2020). High active material loading in all-solid-state battery electrode via particle size optimization. Adv. Energy Mater. *10*, 1902881.
22. Han, Y., Jung, S.H., Kwak, H., Jun, S., Kwak, H.H., Lee, J.H., Hong, S., and Jung, Y.S. (2021). Single- or poly-crystalline Ni-rich layered cathode, sulfide or halide solid electrolyte: which will be the winners for all-solid-state batteries? Adv. Energy Mater. *11*, 2100126.
23. Strauss, F., Bartsch, T., de Biasi, L., Kim, A.Y., Janek, J., Hartmann, P., and Brezesinski, T. (2018). Impact of cathode material particle size on the capacity of bulk-type all-solid-state batteries. ACS Energy Lett *3*, 992–996.
24. Kwak, H., Han, D., Lyoo, J., Park, J., Jung, S.H., Han, Y., Kwon, G., Kim, H., Hong, S., Nam, K., et al. (2021). New cost-effective halide solid electrolytes for all-solid-state batteries: mechanochemically prepared Fe3+-substituted Li2ZrCl6. Adv. Energy Mater. *11*, 2003190.
25. Ye, L., and Li, X. (2021). A dynamic stability design strategy for lithium metal solid state batteries. Nature *593*, 218–222.
26. Zahiri, B., Patra, A., Kiggins, C., Yong, A.X.B., Ertekin, E., Cook, J.B., and Braun, P.V. (2021). Revealing the role of the cathode–electrolyte interface on solid-state batteries. Nat. Mater. *20*, 1392–1400. https://doi.org/10.1038/s41563-021-01016-0.
27. Koerver, R., Aygün, I., Leichtweiß, T., Dietrich, C., Zhang, W., Binder, J.O., Hartmann, P., Zeier, W.G., and Janek, J. (2017). Capacity fade in solid-state batteries: interphase formation and chemomechanical processes in nickel-rich layered oxide cathodes and lithium thiophosphate solid electrolytes. Chem. Mater. *29*, 5574–5582.

28. Koerver, R., Zhang, W., de Biasi, L., Schweidler, S., Kondrakov, A.O., Kolling, S., Brezesinski, T., Hartmann, P., Zeier, W.G., and Janek, J. (2018). Chemo-mechanical expansion of lithium electrode materials - on the route to mechanically optimized all-solid-state batteries. Energy Environ. Sci. *11*, 2142–2158.

29. Wang, C., Hwang, S., Jiang, M., Liang, J., Sun, Y., Adair, K., Zheng, M., Mukherjee, S., Li, X., Li, R., et al. (2021). Deciphering interfacial chemical and electrochemical reactions of sulfide-based all-solid-state batteries. Adv. Energy Mater. *11*, 2100210.

30. Li, X., Liang, J., Chen, N., Luo, J., Adair, K.R., Wang, C., Banis, M.N., Sham, T.K., Zhang, L., Zhao, S., et al. (2019). Water-mediated synthesis of a superionic halide solid electrolyte. Angew. Chem. Int. Ed. Engl. *58*, 16427–16432.

31. Li, X., Liang, J., Yang, X., Adair, K.R., Wang, C., Zhao, F., and Sun, X. (2020). Progress and perspectives on halide lithium conductors for all-solid-state lithium batteries. Energy Environ. Sci. *13*, 1429–1461.

32. Wu, E.A., Banerjee, S., Tang, H., Richardson, P.M., Doux, J.M., Qi, J., Zhu, Z., Grenier, A., Li, Y., Zhao, E., et al. (2021). A stable cathode-solid electrolyte composite for high-voltage, long-cycle-life solid-state sodium-ion batteries. Nat. Commun. *12*, 1256.

33. Li, X., Liang, J., Luo, J., Norouzi Banis, M., Wang, C., Li, W., Deng, S., Yu, C., Zhao, F., Hu, Y., et al. (2019). Air-stable Li_3InCl_6 electrolyte with high voltage compatibility for all-solid-state batteries. Energy Environ. Sci. *12*, 2665–2671.

34. Doerrer, C., Capone, I., Narayanan, S., Liu, J., Grovenor, C.R.M., Pasta, M., and Grant, P.S. (2021). High energy density single-crystal NMC/Li_6PS_5Cl cathodes for all-solid-state lithium-metal batteries. ACS Appl. Mater. Interfaces *13*, 37809–37815.

35. Riegger, L.M., Schlem, R., Sann, J., Zeier, W.G., and Janek, J. (2021). Lithium-metal anode instability of the superionic halide solid electrolytes and the implications for solid-state batteries. Angew. Chem. Int. Ed. Engl. *60*, 6718–6723.

36. Park, K.H., Kaup, K., Assoud, A., Zhang, Q., Wu, X., and Nazar, L.F. (2020). High-voltage superionic halide solid electrolytes for all-solid-state Li-ion batteries. ACS Energy Lett. *5*, 533–539.

37. Zhou, L., Kwok, C.Y., Shyamsunder, A., Zhang, Q., Wu, X., and Nazar, L.F. (2020). A new halospinel superionic conductor for high-voltage all solid state lithium batteries. Energy Environ. Sci. *13*, 2056–2063.

38. Liang, J., Li, X., Wang, S., Adair, K.R., Li, W., Zhao, Y., Wang, C., Hu, Y., Zhang, L., Zhao, S., et al. (2020). Site-occupation-tuned superionic Li_xScCl_{3+x} halide solid electrolytes for all-solid-state batteries. J. Am. Chem. Soc. *142*, 7012–7022.

39. Noh, H.J., Youn, S., Yoon, C.S., and Sun, Y.K. (2013). Comparison of the structural and electrochemical properties of layered Li [NixCoyMnz]O2 (x = 1/3, 0.5, 0.6, 0.7, 0.8 and 0.85) cathode material for lithium-ion batteries. J. Power Sources *233*, 121–130.

40. Levasseur, S., Ménétrier, M., and Delmas, C. (2002). On the dual effect of Mg doping in $LiCoO_2$ and $Li_{1+\delta}CoO_2$: structural, electronic properties, and ^{7}Li MAS NMR studies. Chem. Mater. *14*, 3584–3590.

41. Schlem, R., Banik, A., Ohno, S., Suard, E., and Zeier, W.G. (2021). Insights into the lithium sub-structure of superionic conductors Li_3YCl_6 and Li_3YBr_6. Chem. Mater. *33*, 327–337.

42. Flores-González, N., Minafra, N., Dewald, G., Reardon, H., Smith, R.I., Adams, S., Zeier, W.G., and Gregory, D.H. (2021). Mechanochemical synthesis and structure of lithium tetrahaloaluminates, $LiAlX_4$ (X = Cl, Br, I): a family of Li-ion conducting ternary halides. ACS Materials Lett. *3*, 652–657.

43. Tanibata, N., Takimoto, S., Nakano, K., Takeda, H., Nakayama, M., and Sumi, H. (2020). Metastable chloride solid electrolyte with high formability for rechargeable all-solid-state lithium metal batteries. ACS Materials Lett. *2*, 880–886.

44. Doux, J.M., Yang, Y., Tan, D.H.S., Nguyen, H., Wu, E.A., Wang, X., Banerjee, A., and Meng, Y.S. (2020). Pressure effects on sulfide electrolytes for all solid-state batteries. J. Mater. Chem. A *8*, 5049–5055.

45. Shi, X., Zeng, Z., Zhang, H., Huang, B., Sun, M., Wong, H.H., Lu, Q., Luo, W., Huang, Y., Du, Y., and Yan, C.H. (2021). Gram-scale synthesis of nanosized Li_3HoBr_6 solid electrolyte for all-solid-state Li-Se battery. Small Methods *5*, 2101002.

46. Cronau, M., Szabo, M., König, C., Wassermann, T.B., and Roling, B. (2021). How to measure a reliable ionic conductivity? The stack pressure dilemma of microcrystalline sulfide-based solid electrolytes. ACS Energy Lett. *6*, 3072–3077.

47. de Biasi, L., Kondrakov, A.O., Geßwein, H., Brezesinski, T., Hartmann, P., and Janek, J. (2017). Between Scylla and Charybdis: balancing among structural stability and energy density of layered NCM cathode materials for advanced lithium-ion batteries. J. Phys. Chem. C *121*, 26163–26171.

Joule, Volume *6*

Supplemental information

Solid-state lithium battery cathodes operating at low pressures

Xiangwen Gao, Boyang Liu, Bingkun Hu, Ziyang Ning, Dominic Spencer Jolly, Shengming Zhang, Johann Perera, Junfu Bu, Junliang Liu, Christopher Doerrer, Ed Darnbrough, David Armstrong, Patrick S. Grant, and Peter G. Bruce

Supplementary Information

Materials and methods

Electrode preparation: All chemicals were dried under vacuum and stored in an Ar-filled glovebox (O_2 and H_2O levels < 1 ppm). All there SEs including Li_3InCl_6, Li_3YCl_6 and $LiAlCl_4$ were prepared by a ball milling method, described in previous studies[1-4]. Stoichiometric ratios of indium chloride ($InCl_3$, Merck, 99.99%), aluminium chloride ($AlCl_3$, Merck, 99.999%) or yttrium chloride (YCl_3, Merck, 99.99%) were mechanically mixed with lithium chloride (LiCl, Sigma, 99.9 %) in a ZrO_2 ball milling. For the composite cathode, single crystal $LiNi_{0.83}Mn_{0.06}Co_{0.11}O_2$ (MSE Supplies), Li_3InCl_6 and carbon nanofiber (CNF) (Merck) with different ratios were mixed in a planetary ball mill (Fritsch Pulverisette 7).

Conductivity measurements: Electrochemical impedance spectroscopy (EIS) was carried out using a Gamry Instruments Interface-1000 potentialstat with a voltage amplitude of 10 mV in the frequency range from 1 MHz to 1 Hz. The solid electrolyte powder was pressed at 500 MPa in the polyether ether ketone (PEEK) mould to make the pellet and two carbon paper or In foils (5 mm diameter, Merck, 99.995%) were pressed on the pellet under 300 MPa[5,6]. EIS measurements were carried out under different external pressures at -20, 30 or 80 ^oC in an Ar-filled glovebox.

Cell assembly: Solid-state cells were assembled in a custom-designed module with a PEEK mould and two stainless steel plungers. The inner diameter is 5 mm. A series of layers comprising 4.5-7 mg of the composite cathode mixture (corresponding to a capacity of 3-5 mAh cm^{-2}), 20 mg of Li_3InCl_6, 20 mg of Li_6PS_5Cl (MSE Supplies), an In foil (5 mm diameter, Merck, 99.995%) and Li foil (5 mm diameter, Merck, 99.9 %) were pressed at 500 MPa for 5 mins. The Li: In mass ratio is 3: 97 and the Li atom ratio in the LiIn alloy is 33%, in accord with previous studies[7]. All work was carried out in an Ar-filled glovebox with O_2 and H_2O level below 1 ppm. Galvanostatic cycling was performed at a VMP3 potentiostat (Biologic). We take an average performance of three cells and one standard deviation was used.

Characterization: Power X-ray diffraction (PXRD) measurements were carried out in a Rigaku MiniFlex inside an Ar-filled glovebox. Scanning electron microscopy (SEM) images were taken using a Zeiss-Merlin microscope equipped with energy-dispersive X-ray (EDX) spectroscopy function using an airtight transfer holder without exposure to air. Plasma focused ion beam scanning electron microscopy (PFIB-SEM) section was used to characterize the cross-section morphology of the electrode. PFIB sectioning was performed on a ThermoFisher Helios G4

Plasma-FIB instrument with the Auto Slice function. A stack of SEM images were taken from the cross-sectional surface by serial sectioning at 30 kV and 500 pA and a step size (slice thickness) of 100 nm. The stack images were then processed with an in-house Image J script based on fast Fourier transform (FFT) to remove the curtaining artefact, which originates from the variation of local sputtering rate. The small drift was corrected using the 3D drift correction function by Parslow et al[8]. The resulting new image stack was then cropped and processed by Avizo Fire (2020.3) for 3D visualisation and segmentation.

Mechanical property measurements: The synthesised Li_3InCl_6 powder was pressed at 500 MPa to make the pellet. The elastic modulus and hardness were measured on the pellet by the Hysitron PI 88 in-situ nanoindenter equipped with a Berkovich tip under the low loads testing regime using continuous stiffness measurement. Four distinct regions of the pellet were chosen, and 3-5 indents were conducted in each region. During indentation shallow (3 nm in amplitude), high-frequency (160 Hz) oscillations were applied to the nanoindenter tip. The modulus and hardness were calculated based on the unloading curve, using the method developed by Oliver and Pharr[9]. For the indents in each region, the mean modulus/hardness data is taken to produce a plot of modulus/hardness vs depth. The mode is taken as the value for the elastic modulus and harness of the Li_3InCl_6 sample with the standard error calculated from the variance and the number of tests conducted in each region.

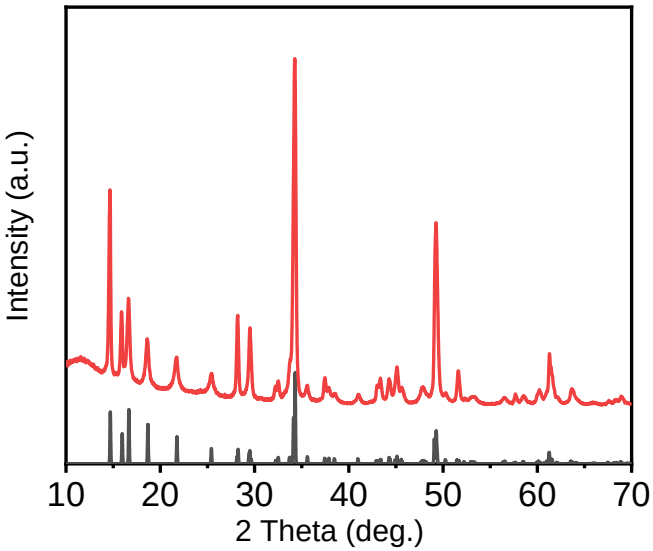

Figure S1. PXRD of the synthesised Li_3InCl_6 (red) and Li_3InCl_6 standard (black).

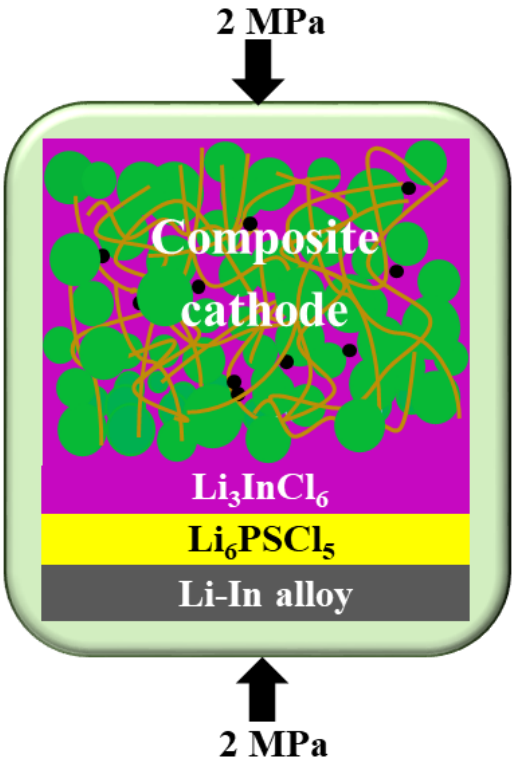

Figure S2. Schematic of the solid-state cell comprising a composite cathode, a layer of Li_3InCl_6, a layer of Li_6PS_5Cl and a Li-In alloy.

Table S1. Comparisons of the mechanical properties of different families of solid electrolytes

Solid electrolytes	Elastic Modulus (GPa)	Hardness (GPa)	Ref
Garnet-type (LLZO)	140-155	8-10	10–13
LLTO	150-220	8-10	11, 14
Li_6PS_5Cl calculated	22	/	15
Li_3InCl_6	34.2 ± 0.8	2.07 ± 0.10	This work
Li_3MCl_6 (M=Sc, Y, Nd, *etc.*) calculated	38-47	/	16

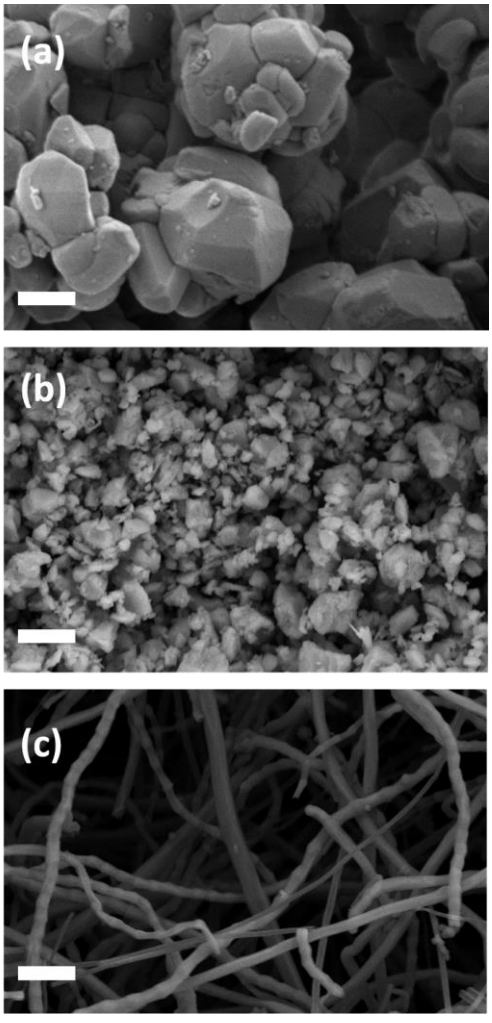

Figure S3. SEM images of (a) $LiNi_{0.83}Mn_{0.06}Co_{0.11}O_2$, (b) synthesised Li_3InCl_6 particles, and (c) CNF. The scale bar is 1 μm.

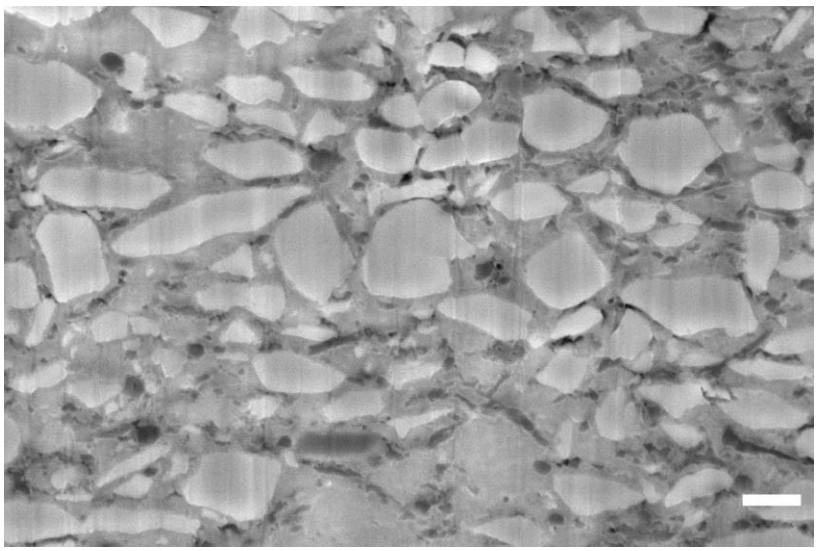

Figure S4. Cross-sectional SEM image of the composite cathode. The scale bar is 1 µm.

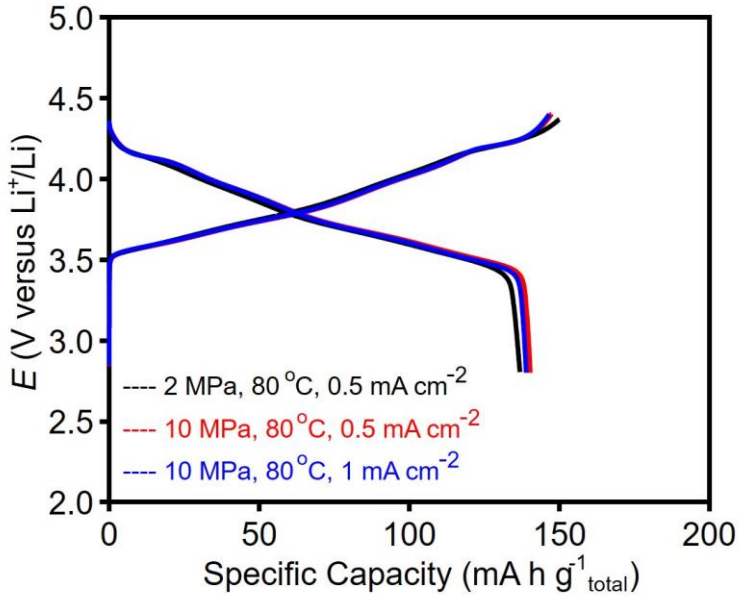

Figure S5. Load curves for the 1st cycle of the composite cathode tested at 80 °C with: (black) 2 MPa, 0.5 mA cm^{-2}; (blue) 10 MPa, 1 mA cm^{-2} and (red) 10 MPa, 0.5 mA cm^{-2}. The CAM, SE, and CNF mass ratios are 65 wt%, 30 wt% and 5 wt%, respectively.

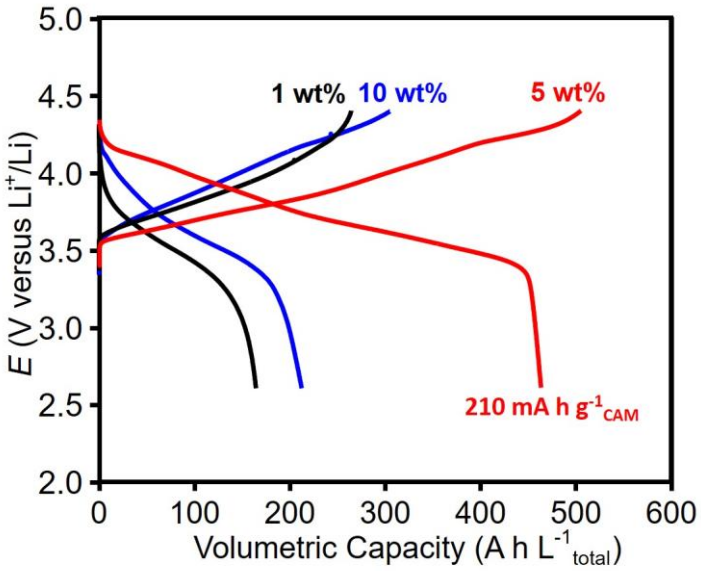

Figure S6. Load curves for the 1st cycle of the composite cathode with different CNF mass ratios: 1 wt% (black), 5 wt% (red) and 10 wt% (blue) under 2 MPa at 80 °C. The current density is 1 mA cm^{-2}. Mass ratio of CAM to SE is constant at 13: 6. The volumetric capacity is calculated based on the volume of the total composite cathode.

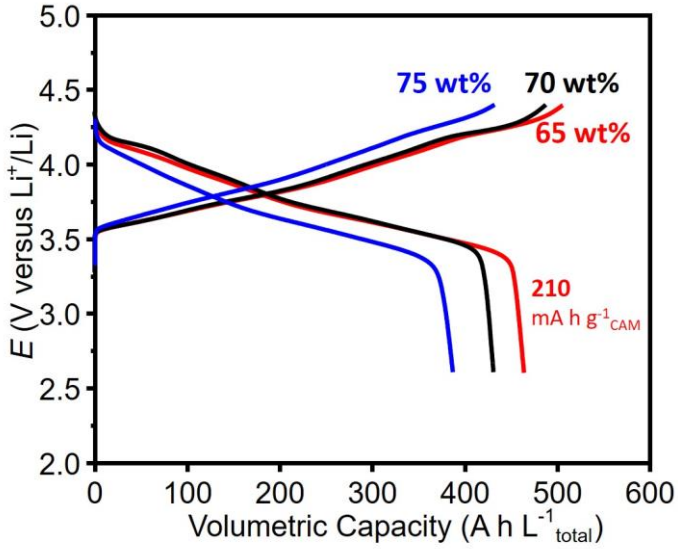

Figure S7. Load curves for the 1st cycle of the composite cathode with different CAM mass ratios: 65 wt% (red), 70 wt% (black) and 75 wt% (blue) under 2 MPa at 80 °C. The carbon ratio is fixed at 5 wt%. The current density is 1 mA cm^{-2}. The volumetric capacity is calculated based on the volume of the total composite cathode.

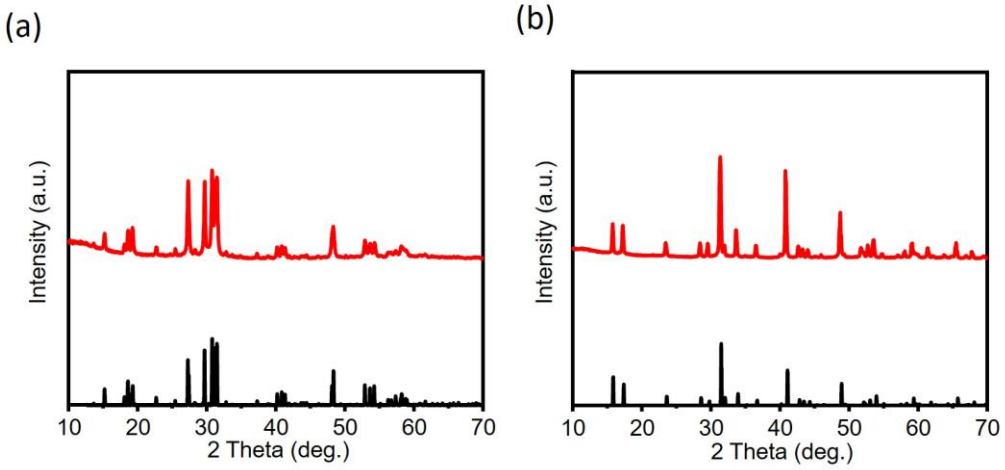

Figure S8. PXRD of the synthesized (a) $LiAlCl_4$ and (b) Li_3YCl_6 (red) and their standard references.

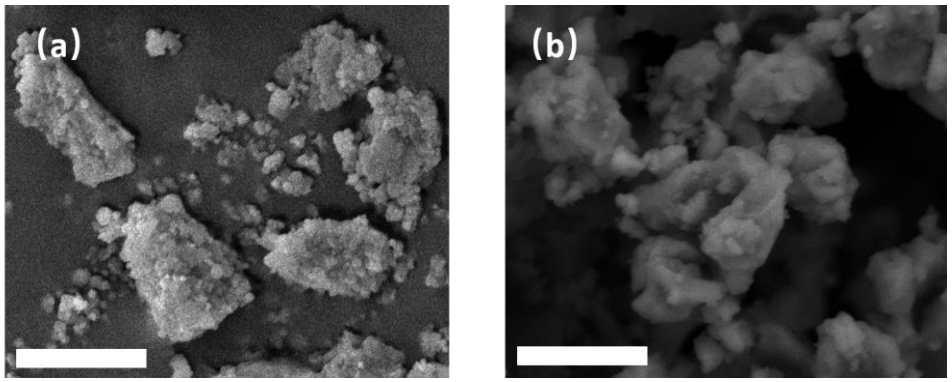

Figure S9. SEM images of (a) $LiAlCl_4$ and (b) Li_3YCl_6. The scale bar is 1 μm.

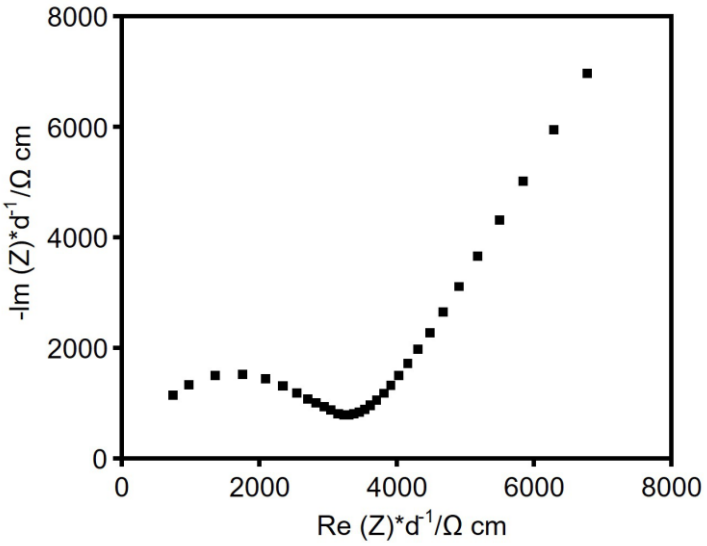

Figure S10. The Nyquist plot of the symmetric C|Li_3InCl_6|C cell measured under 2 MPa stack pressure at -20 °C.

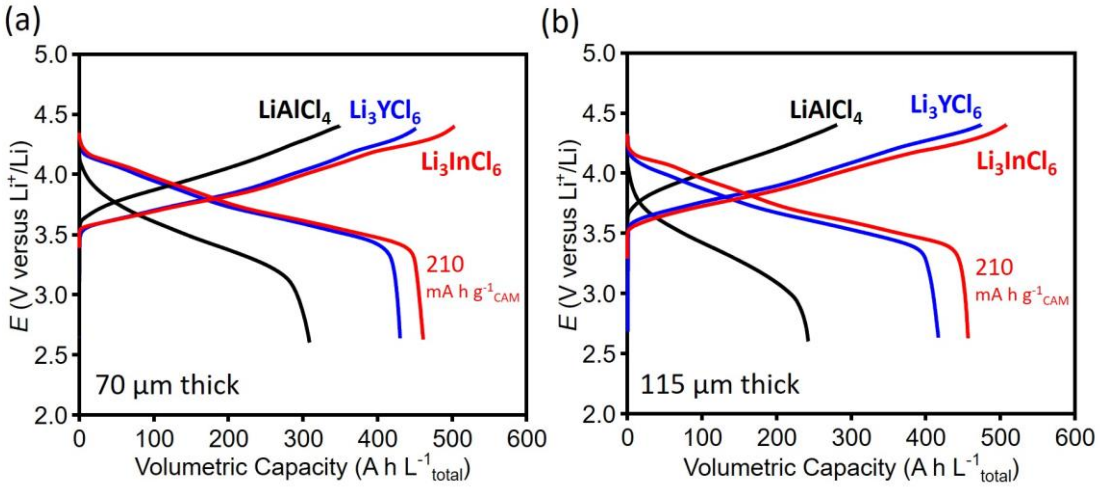

Figure S11. Load curves of the 1st cycle of the composite cathode with various SEs: Li_3InCl_6 (red), Li_3YCl_6 (blue) and $LiAlCl_4$ (black) under 2 MPa at 80 °C. The current density is 1 mA cm^{-2}. The volumetric capacity is calculated based on the volume of the total composite cathode. IR compensations are applied. The CAM, SE, and CNF volume ratios are 49 %, 41 % and 10 %, respectively. The loading thickness is (a) 70 µm and (b) 115 µm.

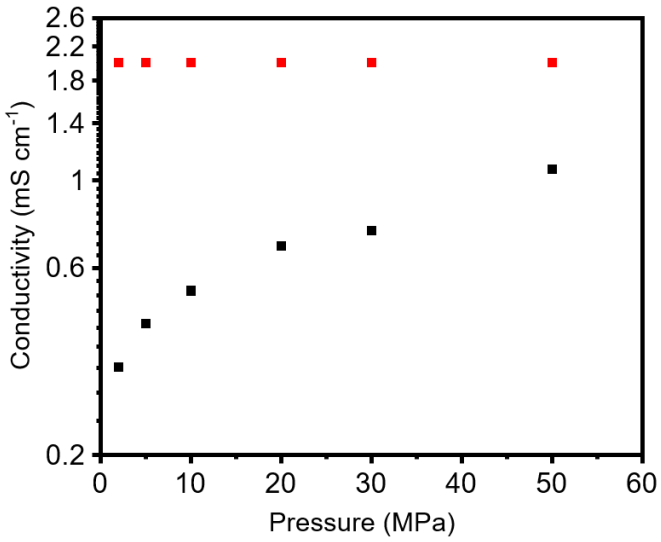

Figure S12. The conductivity of the Li_3InCl_6 (black) and (Li_6PS_5Cl) pellet under different stack pressures at 30 °C.

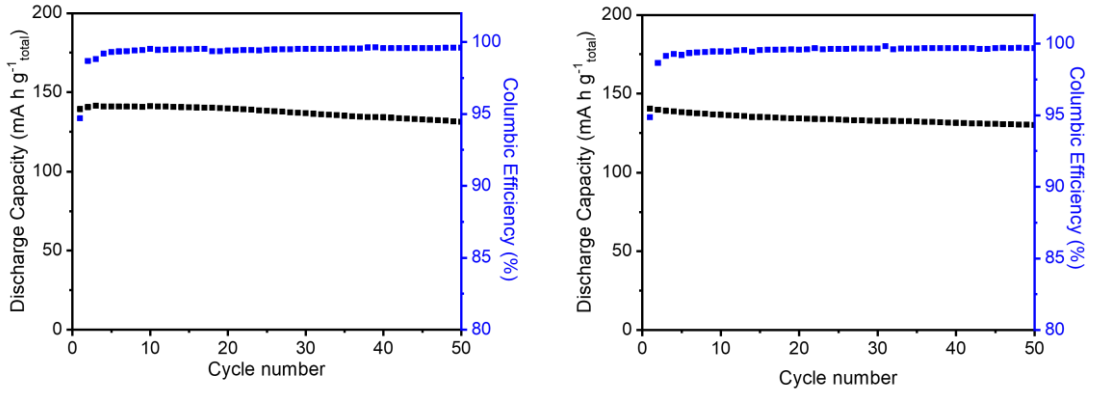

Figure S13. Replicate of the cycling performance of the composite cathode between 2.6 and 4.4 V under 10 MPa at 80 °C. The current density is 1 mA cm^{-2}. The average capacity is 141 ± 0.6 mA h g^{-1}_{total}.

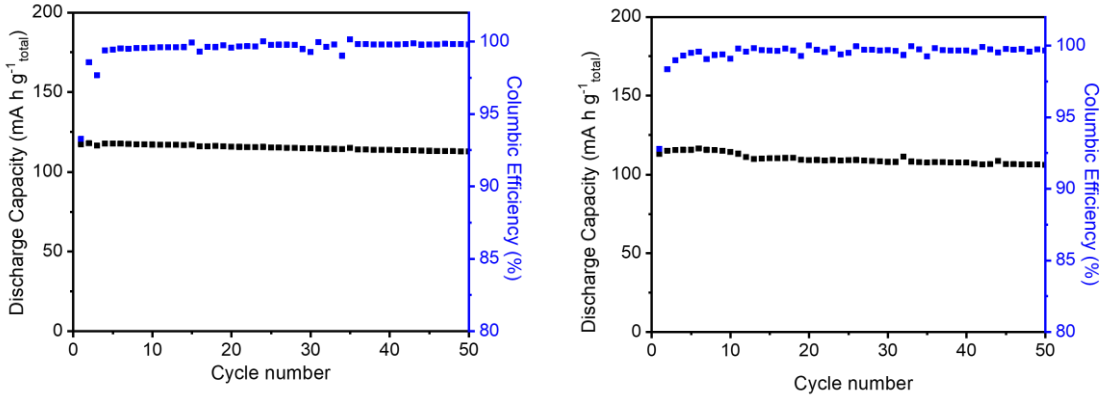

Figure S14. Replicate of the cycling performance of the composite cathode between 2.6 and 4.2 V under 2 MPa at 80 °C. The current density is 1 mA cm^{-2}.

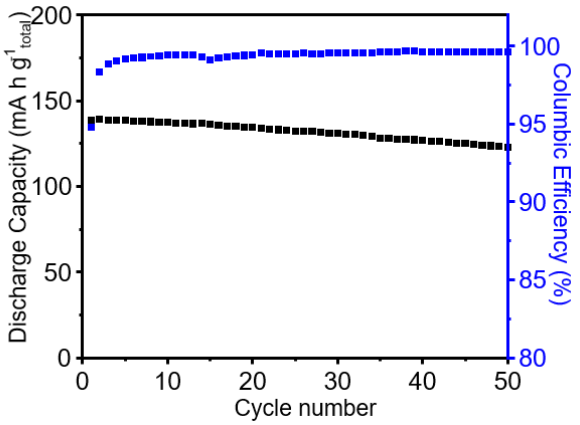

Figure S15. Cycling performance of the composite cathode between 2.6 and 4.4 V (15 mins voltage hold at 4.4 V) under 2 MPa at 80 °C. The current density is 1 mA cm^{-2}. The CAM, SE, and CNF mass ratios are 65 wt%, 30 wt% and 5 wt%, respectively.

References

1. Li, X., Liang, J., Luo, J., Norouzi Banis, M., Wang, C., Li, W., Deng, S., Yu, C., Zhao, F., Hu, Y., et al. (2019). Air-stable Li_3InCl_6 electrolyte with high voltage compatibility for all-solid-state batteries. Energy Environ. Sci. *12*, 2665–2671.

2. Flores-González, N., Minafra, N., Dewald, G., Reardon, H., Smith, R.I., Adams, S., Zeier, W.G., and Gregory, D.H. (2021). Mechanochemical Synthesis and Structure of Lithium Tetrahaloaluminates, LiAlX4 (X = Cl, Br, I): A Family of Li-Ion Conducting Ternary Halides. ACS Mater. Lett. *3*, 652–657.

3. Tanibata, N., Takimoto, S., Nakano, K., Takeda, H., Nakayama, M., and Sumi, H. (2020). Metastable Chloride Solid Electrolyte with High Formability for Rechargeable All-Solid-State Lithium Metal Batteries. ACS Mater. Lett. *2*, 880–886.

4. Schlem, R., Banik, A., Ohno, S., Suard, E., and Zeier, W.G. (2021). Insights into the Lithium Sub-structure of Superionic Conductors Li3YCl6 and Li3YBr6. Chem. Mater. *33*, 327–337.

5. Jean-Marie Doux, Yangyuchen Yang, S. Tan, D.H., Han Nguyen, A. Wu, E., Xuefeng Wang, Abhik Banerjee, and Shirley Meng, Y. (2020). Pressure effects on sulfide electrolytes for all solid-state batteries. J. Mater. Chem. A *8*, 5049–5055.

6. Shi, X., Zeng, Z., Zhang, H., Huang, B., Sun, M., Wong, H.H., Lu, Q., Luo, W., Huang, Y., Du, Y., et al. (2021). Gram-Scale Synthesis of Nanosized Li3HoBr6 Solid Electrolyte for All-Solid-State Li-Se Battery. Small Methods *5*, 2101002.

7. Santhosha, A.L., Medenbach, L., Buchheim, J.R., and Adelhelm, P. (2019). The Indium–Lithium Electrode in Solid-State Lithium-Ion Batteries: Phase Formation, Redox Potentials, and Interface Stability. Batter. Supercaps *2*, 524–529.

8. Parslow, A., Cardona, A., and Bryson-Richardson, R.J. (2014). Sample Drift Correction Following 4D Confocal Time-lapse Imaging. J. Vis. Exp. *86*, 51086.

9. Oliver, W.C., and Pharr, G.M. (2004). Measurement of hardness and elastic modulus by instrumented indentation: Advances in understanding and refinements to methodology. J. Mater. Res. *19*, 3–20.

10. Kim, Y., Jo, H., Allen, J.L., Choe, H., Wolfenstine, J., and Sakamoto, J. (2016). The Effect of Relative Density on the Mechanical Properties of Hot-Pressed Cubic $Li_7La_3Zr_2O_{12}$. J. Am. Ceram. Soc. *99*, 1367–1374.

11. Wolfenstine, J., Allen, J.L., Sakamoto, J., Siegel, D.J., and Choe, H. (2018). Mechanical behavior of Li-ion-conducting crystalline oxide-based solid electrolytes: a brief review. Ionics. *24*, 1271–1276.

12. Han, G., Kinzer, B., Garcia-Mendez, R., Choe, H., Wolfenstine, J., and Sakamoto, J. (2020). Correlating the effect of dopant type (Al, Ga, Ta) on the mechanical and electrical properties of hot-pressed Li-garnet electrolyte. J. Eur. Ceram. Soc. *40*, 1999–2006.

13. Krauskopf, T., Richter, F.H., Zeier, W.G., and Janek, J. (2020). Physicochemical Concepts of the Lithium Metal Anode in Solid-State Batteries. Chem. Rev. *120*, 7745–7794.

14. Cho, Y.-H., Wolfenstine, J., Rangasamy, E., Kim, H., Choe, H., and Sakamoto, J. (2012). Mechanical properties of the solid Li-ion conducting electrolyte: $Li_{0.33}La_{0.57}TiO_3$. J. Mater. Sci. *47*, 5970–5977.

15. Deng, Z., Wang, Z., Chu, I.-H., Luo, J., and Ong, S.P. (2016). Elastic Properties of Alkali Superionic Conductor Electrolytes from First Principles Calculations. J. Electrochem. Soc. *163*, A67.

16. Ming Jiang, Sankha Mukherjee, Wen Chen, Z., Xin Chen, L., Lu Li, M., Yan Xiao, H., Chan Gao, and Veer Singh, C. (2020). Materials perspective on new lithium chlorides and bromides: insights into thermo-physical properties. Phys. Chem. Chem. Phys. *22*, 22758–22767.